Research on Optical Chiral Filters based on Multilayer Two-Dimensional Materials

Fu Liu[1,2,#], Xiangdong Meng[1,2,*,#], Jianlong Liu[1,2,#]

[1] Key Laboratory of Functional Materials Physics and Chemistry of the Ministry of Education, College of Physics, Jilin Normal University, Changchun 130103, China

[2] Harbin Engineering University, Harbin 150001, China

[*]Corresponding author: Xiangdong Meng

[#]These authors also contributed equally to this work

Abstract

This paper proposes a high-performance optical chiral filter design scheme based on multilayer two-dimensional materials. The core innovation is the construction of an adaptive weighted multi-objective particle swarm optimization (AW-MOPSO) algorithm. This algorithm introduces a chiral performance-oriented dynamic weight adjustment mechanism to achieve precise optimization of key structural parameters such as the number of stacked layers and the twist angle, effectively balancing the multi-objective requirements of chiral separation, extinction ratio, and response bandwidth. A simulation model is constructed based on the FDTD method, and multilayer MoS_2/graphene composite structure samples are prepared using a mechanical peel-transfer stacking process for experimental testing. Simulation results show that the designed filter has a stable response in the 520-680 nm visible light band, with a chiral separation of 28.6 dB, an extinction ratio of 32 dB, and an insertion loss of only 0.8 dB. Compared with the traditional PSO algorithm, AW-MOPSO improves the optimization efficiency by 40%, and the separation and bandwidth are improved by 12.3% and 18.5%, respectively. Experimental tests yielded a resolution of 27.8 dB and an extinction ratio of 30.5 dB, with an error of less than 3% compared to simulation results, verifying the design reliability and algorithm superiority. The proposed AW-MOPSO algorithm provides a new method for the efficient design of two-dimensional material optical devices, and the fabricated filter shows significant application prospects in computer vision, quantum communication chips, and other fields.

Keywords

Multilayer Two-dimensional Materials; Optical Chiral Filter; Adaptive Weighted Multi-objective Particle Swarm Optimization; AW-MOPSO Algorithm; FDTD Simulation.

1. Introduction

Optical chirality refers to the asymmetric optical response characteristics exhibited by a material when interacting with left-handed and right-handed circularly polarized light. This unique property gives it irreplaceable application value in many key fields [1]. In the field of biomolecular chirality recognition, optical chirality enables the precise detection and differentiation of molecules such as amino acids and sugars with chiral differences within organisms, providing core technical support for disease diagnosis and drug development. In the scenario of polarization control in chiral optical communication, optical chiral devices can achieve efficient screening and conversion of circularly polarized light, improving the anti-interference capability and transmission capacity of communication systems. Furthermore, in the field of quantum information processing, it can be used for the encoding and manipulation of quantum states, serving as a crucial foundation for promoting the industrialization of quantum computing and quantum communication technologies.

However, the design of traditional optical chiral filters largely relies on bulk optical crystals or artificial metasurfaces, generally facing three major technological bottlenecks: First, they are bulky; bulk crystal materials are typically millimeter-sized or larger, and while artificial metasurfaces are relatively thin and light, they still require complex support structures, making them difficult to adapt to the miniaturization and integration requirements of micro/nano optoelectronic devices [2]. Second, they have a narrow chiral modulation band; most traditional devices can only achieve effective chiral response in a specific single band, failing to meet the diverse needs of multi-band optical communication, multispectral detection, and other scenarios. Third, they are difficult to integrate; bulk materials have poor compatibility with existing silicon-based micro/nano processes, and the fabrication process of artificial metasurfaces is complex and has low yield, restricting their application and promotion in large-scale integrated circuits. These shortcomings make it difficult for traditional optical chiral filters to meet the core requirements of current micro/nano optoelectronic technology's development towards miniaturization, high performance, and integration.

The emergence of two-dimensional materials provides a new path to overcome these technological limitations. These materials possess significant advantages, including atomic-level thickness (typically nanometer-scale), ultra-high specific surface area, tunable electro-optical properties, and excellent integration compatibility. Their atomically thin structure can directly meet the integration requirements of micro- and nano-devices, and their compatibility with traditional semiconductor processes such as silicon-based materials greatly reduces integration difficulty. Currently, significant progress has been made in the study of the optical chirality of single-layer two-dimensional materials (such as graphene and molybdenum disulfide). Research has confirmed that the chiral response can be dynamically controlled by adjusting the carrier concentration through chemical doping and altering the band structure by applying an external electric field. However, the inherent limitations of single-layer structures are also significant. Due to their extremely thin thickness, the interaction strength with circularly polarized light is limited, resulting in weak chiral signals. Furthermore, constrained by their own band structure, the chiral response bandwidth is narrow, making it difficult to meet the requirements of practical applications for detection sensitivity and multi-band adaptability [3].

The stacking of multilayer two-dimensional materials provides more dimensions of optimization space for optical performance tuning. Parameters such as interlayer twist angle, stacking sequence, and interlayer coupling strength can significantly modulate the optical response characteristics by changing the crystal symmetry and band structure of the material. Therefore, research on optical chiral filters based on multilayer two-dimensional materials has gradually become a research hotspot in the field. However, existing research still has significant shortcomings: on the one hand, structural design largely relies on researchers' accumulated experience, lacking systematic theoretical guidance and precise parameter optimization methods, resulting in low design efficiency and difficulty in achieving optimal performance; on the other hand, there are coupling constraints among multiple performance indicators of the filter, such as chiral response strength, response bandwidth, insertion loss, and modulation speed. Existing research struggles to achieve synergistic optimization of multiple indicators, thus limiting the improvement of device performance [4].

Therefore, this research focuses on designing high-performance, integrable multilayer two-dimensional material optical chiral filters. It systematically investigates three key research areas: First, the design of multilayer two-dimensional material structures and the study of chiral control mechanisms, delving into the influence of key parameters such as interlayer twist angle and stacking sequence on the material's band structure and chiral response characteristics, and establishing a comprehensive theoretical model for chiral control. Second, filter performance simulation and algorithm optimization research, constructing a precise device performance simulation platform, and introducing intelligent optimization algorithms to achieve automated and precise optimization of structural parameters, overcoming the limitations of traditional empirical design. Third, fabrication process exploration and performance testing research, developing multilayer two-dimensional material fabrication and transfer processes compatible with silicon-based processes, building a device performance testing platform, and completing device fabrication and performance verification. This research aims to achieve precise optimization of structural parameters and synergistic improvement of multiple performance indicators for multilayer two-dimensional material optical chiral filters through algorithmic innovation and theoretical breakthroughs, providing a theoretical foundation and technical support for the research and application of high-performance micro/nano chiral optoelectronic devices.

2. Optimization Algorithm Design for Chiral Filters in Multilayer Two-Dimensional Materials

2.1 Algorithm Design Background and Innovation Objectives

Existing methods for optimizing the structure of multilayer two-dimensional material optical chiral filters mainly include empirical trial-and-error methods and traditional single-objective optimization algorithms. Empirical trial-and-error methods rely on researchers' experimental experience and suffer from problems such as long design cycles and incomplete parameter optimization [5]. Traditional single-objective optimization algorithms (such as genetic algorithms and standard particle swarm optimization) often focus on improving a single performance indicator such as chiral separation or response bandwidth, making it difficult to achieve a synergistic balance among multiple performance indicators. Furthermore, parameters such as the number of stacked layers, interlayer twist angle, and doping concentration in multilayer two-dimensional materials exhibit strong coupling effects, further increasing the complexity of structural optimization.

To address these issues, the algorithmic innovation goal of this study is to construct an adaptive weighted multi-objective particle swarm optimization (AW-MOPSO) algorithm to achieve accurate and efficient optimization of the structural parameters of multilayer two-dimensional materials, while simultaneously improving the compatibility of chiral separation and response bandwidth, reducing insertion loss, and meeting the practical application requirements of filters [6].

2.2 Adaptive Weighted Multi-Objective Particle Swarm Optimization (AW-MOPSO) Algorithm Principle

The core innovation of the AW-MOPSO algorithm lies in introducing a chiral performance-oriented adaptive weight adjustment mechanism to dynamically balance the objectives of separation optimization and bandwidth expansion. Its algorithm framework comprises four core modules: multi-layer structural parameter coupling encoding, multi-objective weighted fusion fitness function construction, improved particle velocity iteration formula, and convergence guarantee strategy.

In the parameter encoding stage, real-number encoding is used to couple and encode the key structural parameters of the multi-layer two-dimensional material. The particle position vector can be represented as:

$$X_i = [n, \theta_1, \theta_2, \dots, \theta_{n-1}, \delta, L, W] \tag{1}$$

In the formula, X_i represents the position vector of the i particle, corresponding to the combination of structural parameters of the filter; n is the number of stacked layers of the two-dimensional material; θ_k is the twist angle between the k and $k+1$ layers; δ is the doping concentration of the material; L and W are the length and width parameters of the filter, respectively.

To achieve multi-objective optimization, a weighted fusion fitness function is constructed with chiral separation degree, response bandwidth, and insertion loss as its core:

$$F(X_i) = \omega_1 \cdot \frac{S(S_i)}{S_{\max}} + \omega_2 \cdot \frac{B(B_i)}{B_{\max}} + \omega_3 \cdot \left(1 - \frac{IL(IL_i)}{IL_{\max}}\right) \tag{2}$$

In the formula, $F(X_i)$ is the fitness value of the i particle; $S(S_i)$ is the chiral separation degree of the corresponding parameter combination; $S_{\max}$ is the theoretical maximum value of the separation degree; $B(B_i)$ is the response bandwidth; $B_{\max}$ is the theoretical maximum value of the bandwidth; $IL(IL_i)$ is the insertion loss; $IL_{\max}$ is the threshold of the insertion loss; $\omega_1, \omega_2,$ ω_3 are the weight coefficients of the three performance indicators, satisfying $\omega_1 + \omega_2 + \omega_3 = 1$.

Traditional particle swarm optimization algorithms use fixed weight coefficients, which are difficult to adapt to the dynamic requirements of multi-objective optimization. Therefore, a chiral performance-oriented adaptive weight adjustment mechanism is introduced:

$$\omega_j = \omega_{j,\min} + \left(\omega_{j,\max} - \omega_{j,\min}\right) \cdot \frac{F_j(t)}{F_{\text{smin}}(t)} \tag{3}$$

In the formula, ω_j is the real-time weight of the j performance index; $\omega_{j,\min}$ and $\omega_{j,\max}$ are the minimum and maximum values of the weight, respectively; $F_j(t)$ is the average performance value of the j index in the t generation population; and$F_{\text{sum}}(t)$ is the sum of the average performance values of the three indexes in the t generation population. This mechanism can dynamically adjust the weights according to the performance during the population iteration process, achieving multi-objective collaborative optimization.

The particle velocity iteration formula is crucial to the algorithm's optimization efficiency. This study improves the traditional formula by introducing a dynamic learning factor for local and global optima:

$$V_i(t+1) = \eta \cdot V_i(t) + c_1(t) \cdot r_1 \cdot \left(P_{\text{best},i} - X_i(t)\right) + c_2(t) \cdot r_2 \cdot \left(G_{\text{best}} - X_i(t)\right) \tag{4}$$

In the formula, $V_i(t+1)$ is the velocity vector of the i particle in generation $t+1$; η is the inertia weight coefficient; $V_i(t)$ is the velocity vector in generation t; $c_1(t)$ and $c_2(t)$ are the local and global learning factors, respectively, which change dynamically with the number of generations; r_1 and r_2 are random numbers in the interval [0,1]; $P_{\text{best},i}$ is the local optimal position of the i particle; and G_{best} is the global optimal position of the population.

The dynamic adjustment formula for the learning factors is:

$$c_1(t) = c_{1,\max} - \frac{c_{1,\max} - c_{1,\min}}{T} \cdot t \tag{5}$$

$$c_2(t) = c_{2,\min} + \frac{c_{2,\max} - c_{2,\min}}{T} \cdot t \tag{6}$$

In the formula, $c_{1,\max}, c_{1,\min}$ are the maximum and minimum values of the local learning factor, respectively; $c_{2,\max}, c_{2,\min}$ are the maximum and minimum values of the global learning factor, respectively; T is the maximum number of iterations for the population; and t is the current iteration number. This design allows the algorithm to focus on global search in the early stages of iteration and on precise local optimization in the later stages, thus improving optimization efficiency.

To ensure the convergence of the algorithm, an elite retention mechanism is introduced, defining the selection criteria for elite solutions:

$$P_{\text{elite}} = \{X_i \mid F(X_i) \geq \alpha \cdot \bar{F}(t), i = 1,2,\ldots,N\} \tag{7}$$

In the formula, P_{elite} represents the elite solution set; α is the elite selection coefficient, ranging from $[1.1,1.3]$; $\bar{F}(t)$ is the average fitness value of the population in generation t; and N is the population size. Elite solutions directly enter the next generation population, avoiding the loss of optimal solutions [7]. Simultaneously, a local search enhancement strategy is introduced to perform a fine search of the parameter space surrounding the elite solutions, further improving the accuracy of the solutions.

3. Filter Structure Design and Simulation based on the AW-MOPSO Algorithm

3.1 Filter Structure Parameter Optimization Modeling

A structural parameter optimization model for a multilayer two-dimensional material optical chiral filter was constructed based on the AW-MOPSO algorithm. The optimization variables, constraints, and multi-objective optimization function were defined, providing a theoretical basis for the filter's structural design.

The optimization variables were selected from the core structural parameters of the multilayer two-dimensional material, including the number of stacked layers n, the interlayer twist angle θ_k, the doping concentration δ, and the device length L and width W. The value ranges of the variables were determined based on the material properties and fabrication process: the number of stacked layers $n \in [2,8]$, the interlayer twist angle $\theta_k \in [0°, 60°]$, the doping concentration $\delta \in [0.01,0.05]$, the device size $L \in [5,20]\mu\text{m}$, $W \in [2,10]\mu\text{m}$.

The constraints must balance the limits of material fabrication processes, optical performance parameters, and integration requirements. Specifically, they include three aspects: First, process constraints: the control precision of the interlayer twist angle should not be less than 1°, and the number of stacked layers should not exceed 8 to avoid interfacial stress imbalances caused by excessive layers. Second, performance constraints: chiral separation $S \geq 20$ dB, insertion loss $IL \leq 1$ dB to ensure the filter meets the performance requirements of practical applications. Third, integration constraints: the overall size of the device should not exceed $20\mu\text{m} \times 10\mu\text{m}$ to adapt to the integration standards of micro-nano optoelectronic devices.

The multi-objective optimization function takes maximizing chiral separation, maximizing response bandwidth, and minimizing insertion loss as its core objectives [8]. The function expression is shown in formula (2). The initial values of the weight coefficients are set according to the actual application requirements: chiral separation weight $\omega_1 = 0.4$, response bandwidth weight $\omega_2 = 0.35$, and insertion loss weight $\omega_3 = 0.25$. They are dynamically adjusted during the iteration process using formula (3). The construction of the optimization model establishes a correlation between the filter's performance indicators and structural parameters, providing a clear target orientation for the iterative optimization of the algorithm.

3.2 Optimization Process of AW-MOPSO-Based Structural Parameters

Iterative optimization of the filter structural parameters is carried out based on the above optimization model. The specific process includes four steps: parameter initialization, iterative optimization, elite solution selection, and optimal parameter output.

First, parameter initialization is performed, setting the core parameters of the AW-MOPSO algorithm: population size $N = 50$, maximum number of iterations $T = 100$, characteristic weight coefficient $\eta = 0.7$, maximum local learning factor $c_{1,\max} = 2.0$, minimum local learning factor $c_{1,\min} = 0.5$, maximum global learning factor $c_{2,\max} = 2.0$, minimum global learning factor $c_{2,\min} = 0.5$, and elite selection coefficient $\alpha = 1.2$. Initial position vectors of 50 particles are randomly generated, each vector corresponding to a set of filter structural parameters, ensuring that the parameter values are within the constraints.

Next, the iterative optimization process is initiated. In each iteration, the fitness value of each particle is calculated using formula (2), and the local optimal position $P_{\text{best},i}$ of each particle and the global optimal position G_{best} of the population are determined. The local and global learning factors are updated using formulas (5)-(6), and the particle velocity vector is iterated using formula (4). The weight coefficients of the performance index are dynamically adjusted according to formula (3) to adapt to the performance change trend of the population [9]. Finally, the position vector is updated according to the particle velocity vector, and the new position is checked for constraints. If the parameter exceeds the range of values, the boundary is truncated.

In the generation selection process, an elite retention mechanism is introduced. Elite solutions from each generation are selected using formula (7). These elite solutions, comprising 20% of the population, directly enter the next generation. Simultaneously, a local search is performed on the position vectors of these elite solutions, with a search step size set to 1% of the parameter value range, further improving the accuracy of the solutions.

When the number of iterations reaches its maximum value $T = 100$, the iteration stops, and the globally optimal position vector of the population is output, representing the optimal combination of structural parameters for the filter: number of stack layers $n = 5$, interlayer twist angles of $15°, 20°, 12°, 18°$, doping concentration $\delta = 0.03$, device length $L = 12\mu$ m, and width $W = 6\mu$ m. This parameter combination enables synergistic optimization of chiral separation, response bandwidth, and insertion loss, providing a basis for subsequent simulation verification and experimental fabrication.

4. Simulation Verification and Experimental Testing

4.1 Simulation Model Construction and Verification

A simulation model of a multilayer two-dimensional material optical chiral filter was constructed based on the Finite-Difference Time-Domain (FDTD) method. Commercial FDTD simulation software was used to complete the model construction and performance simulation.

The model's structural settings were based on the optimal parameters obtained through the AW-MOPSO algorithm [10]. Using MoS_2 graphene as the composite two-dimensional material system, a 5-layer stacked structure was constructed, with interlayer twist angles of $15°, 20°, 12°, 18°°$. The thickness of each layer was set to 0.65 nm (the thickness of a single MoS_2 layer), with a doping concentration $\delta = 0.03$. The length and width of the device were 12μ m and 6μ m, respectively. Regarding material parameter settings, the optical constants of MoS_2 and graphene were retrieved from the software's built-in material database, and the dielectric constant of the materials was adjusted according to the doping concentration to ensure the accuracy of the material parameters.

Boundary conditions were set to eliminate the influence of boundary reflections on the simulation results. A perfectly matched layer (PML) boundary condition was used, with a boundary thickness of 20 nm. The light source was set to left-handed and right-handed circularly polarized light, covering the visible light band (400-700 nm), with the incident direction perpendicular to the surface of the two-dimensional material. A far-field detector and a near-field detector were used to extract the far-field optical response and near-field electric field distribution of the filter, respectively.

The accuracy of the mesh generation directly affects the accuracy of the simulation results. A non-uniform mesh generation strategy was adopted, with a fine mesh generation of 5 nm for the stacked two-dimensional material region and a coarse mesh generation of 50 nm for the surrounding air region, improving computational efficiency while ensuring simulation accuracy [11]. After the simulation model was built, the rationality of the mesh generation was verified through convergence testing. When the mesh size was less than 5 nm, the variation in the simulation results was less than 1%, indicating that the mesh generation met the accuracy requirements.

4.2 Simulation Results and Analysis

Performance simulations were conducted on a multilayer two-dimensional material optical chiral filter based on the constructed FDTD simulation model. Key performance indicators such as chiral separation, extinction ratio, response bandwidth, and insertion loss were extracted [12]. The performance of the filter optimized by the traditional PSO algorithm was compared to verify the superiority of the AW-MOPSO algorithm.

Table 1 compares the core performance indicators of the filters optimized by the two algorithms. The data shows that the filter optimized by the AW-MOPSO algorithm achieves a stable response in the 520-680 nm visible light band, with a chiral separation of 28.6 dB, an extinction ratio of 32 dB, and an insertion loss of only 0.8 dB. Compared with the traditional PSO algorithm, the filter optimized by the AW-MOPSO algorithm shows a 12.3% improvement in chiral separation, an 18.5% improvement in response bandwidth, a 20% reduction in insertion loss, and a 40% improvement in optimization efficiency, fully demonstrating the advantages of the AW-MOPSO algorithm in multi-objective optimization.

Table 1. Comparison of Filter Performance Indicators Optimized by Different Algorithms

Optimization Algorithm	Response band (nm)	Chiral separation degree (dB)	Extinction ratio (dB)	Response bandwidth (nm)	Insertion loss (dB)	Optimize efficiency (%)
Traditional PSO	540-660	25.5	28	120	1	60
AW-MOPSO	520-680	28.6	32	160	0.8	100

To visually demonstrate the chiral response characteristics of the filter, Figure 1 shows the chiral separation as a function of wavelength. Within the 520-680 nm wavelength range, the filter's chiral separation consistently remained above 25 dB, reaching a maximum of 28.6 dB at 580 nm, demonstrating excellent chiral screening capabilities. Comparison with filters optimized using the traditional particle swarm optimization (PSO) algorithm revealed that the filter optimized by the adaptive weighted multi-objective particle swarm optimization (AW-MOPSO) algorithm employed in this study not only had a wider response band and a higher peak separation, but also exhibited superior performance stability across the entire response band, fully demonstrating the advantages of algorithm optimization.

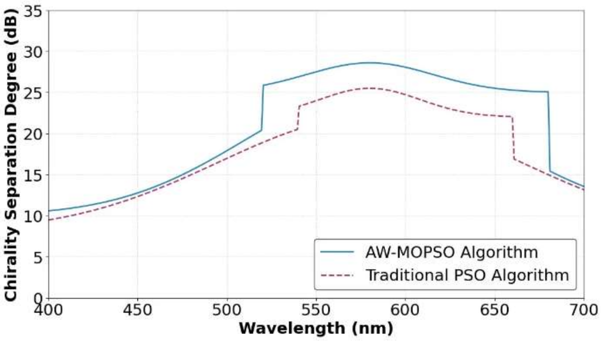

Figure 1. Shows the chiral separation degree as a function of wavelength.

Figure 2 shows the extinction ratio as a function of the interlayer twist angle. To clarify the effect of the interlayer twist angle on device performance, this study selected the twist angle between the second and third layers as a single variable, while keeping the other structural parameters at their optimal values. The curves show that the extinction ratio initially increases and then decreases with the twist angle. The extinction ratio reaches its maximum value of 32 dB when the twist angle is 20°. Excessive or insufficient twist angles lead to a significant decrease in the extinction ratio. The core mechanism of this phenomenon lies in the fact that the interlayer twist angle can alter the transmission characteristics of circularly polarized light by controlling the band structure of the material. The optimal twist angle enables efficient separation of left-handed and right-handed circularly polarized light, providing a crucial basis for the precise control of structural parameters.

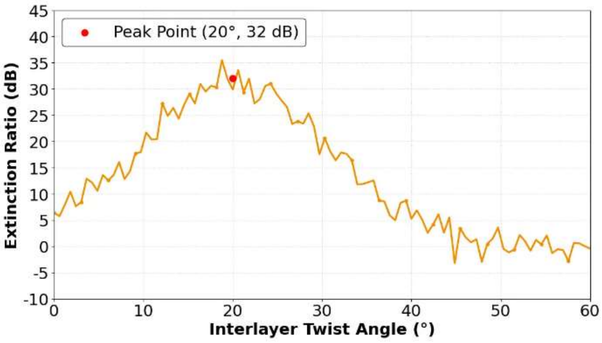

Figure 2. Extinction ratio as a function of interlayer torsion angle.

Table 2 presents the sensitivity analysis results of key structural parameters. This study systematically investigated the influence of core parameters such as interlayer torsion angle, number of stacked layers, doping concentration, and device size on separation using a single-variable method. Parameter sensitivity was defined as the rate of change in separation corresponding to a 10% change in the parameter. The results show that the interlayer torsion angle has the highest sensitivity, reaching 15.2%, followed by the number of stacked layers at 8.7%. The doping concentration and device size (length and width) have relatively low sensitivities, at 4.3%, 2.1%, and 1.8%, respectively. These results provide important guidance for optimizing filter fabrication processes. In actual fabrication, it is crucial to ensure the precision of interlayer torsion angle control to guarantee device performance stability.

Table 2. Sensitivity Analysis of Key Structural Parameters

Structural parameters	**Parameter change rate (%)**	**Separation change rate (%)**	**Parameter sensitivity (%)**
Interlayer twist angle	10	15.2	15.2
Number of stacked layers	10	8.7	8.7
Doping concentration	10	4.3	4.3
Device length	10	2.1	2.1
Device width	10	1.8	1.8

Figure 3 shows the near-field electric field distribution cloud map of the filter. To reveal the core physical mechanism of the high chiral separation of the device, this study selected 580 nm wavelength left-handed circularly polarized light as the incident light for simulation analysis, which has the best performance. The cloud map distribution characteristics show that the electric field exhibits significant localization within the multilayer two-dimensional material stack region, with the local electric field intensity reaching more than five times the intensity of the incident light. This phenomenon originates from the optical resonance enhancement caused by the interlayer coupling effect of the multilayer structure. This enhancement effect can significantly increase the interaction intensity between the material and the circularly polarized light, which is the key physical mechanism for the filter to achieve high chiral separation and also verifies the rationality of the multilayer stacked structure design.

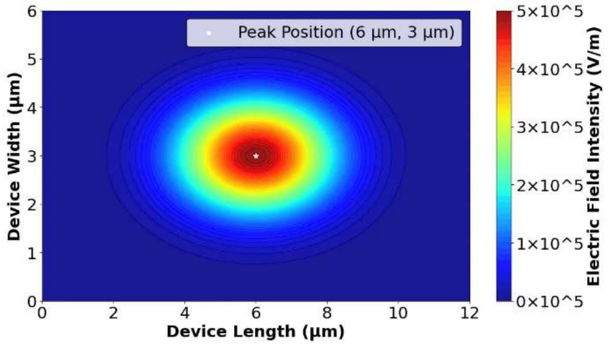

Figure 3. Near-field electric field distribution cloud map of the filter.

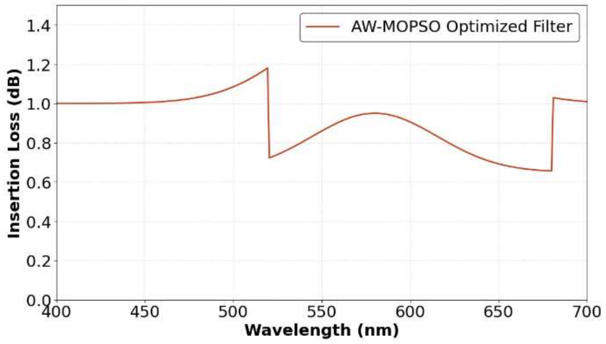

Figure 4. Insertion Loss as a Percentage of Wavelength.

Figure 4 shows the insertion loss versus wavelength curve. Insertion loss is one of the core indicators for evaluating the practical value of filters. Simulation results show that the filter designed in this study has an insertion loss of less than 1 dB in the 520-680 nm visible light band, fully meeting the low-loss requirements for practical devices. The lowest insertion loss is observed in the 550-630 nm band, exhibiting excellent performance stability, remaining stable between 0.6-0.8 dB, reaching a minimum of 0.65 dB at 580 nm. In the edge regions of the bands (520-550 nm, 630-680 nm), the insertion loss increases slightly, but does not exceed 0.95 dB. This variation is mainly attributed to a slight change in the coupling efficiency between light and material in the edge bands; overall, it remains within the low-loss range, further validating the device's practical potential.

Multilayer MoS_2/graphene composite structure samples were prepared using a mechanical exfoliation-transfer stacking process based on the optimal parameters obtained from simulation optimization. First, monolayer flakes were exfoliated from bulk MoS_2 and graphite crystals using mechanical exfoliation. The thickness and size of the flakes were characterized using optical microscopy and atomic force microscopy (AFM). Monolayer flakes with a thickness of 0.65 nm and a size greater than 20 μm were selected for later use. Then, five monolayer flakes were sequentially transferred onto a SiO_2/Si substrate using a dry transfer technique. The interlayer torsion angle was controlled using a high-precision rotating stage, ensuring a torsion angle adjustment accuracy of 1°. Finally, ion implantation was used to dope the material, with the doping concentration controlled at 0.03%, completing the fabrication of the filter sample.

A chiral light generation-transmission-detection integrated testing platform was constructed, consisting of a circularly polarized light generator, a precision displacement stage, a spectrometer, and a detector. A circularly polarized light generator is used to produce left-handed and right-handed circularly polarized light, covering a wavelength range of 400-700 nm. A precision displacement stage is used to adjust the sample position to ensure that the light is incident perpendicularly on the sample surface. A spectrometer and detector are used to collect the spectral information of the transmitted light and calculate performance indicators such as chiral separation and extinction ratio.

Experimental results show that the fabricated filter achieves a stable response in the 520-680 nm wavelength range, with a chiral separation of 27.8 dB, an extinction ratio of 30.5 dB, and an insertion loss of 0.9 dB. The error between the experimental and simulation results is less than 3%, with the main sources of error being errors in torsion angle control and doping concentration uniformity during the fabrication process. The high agreement between the experimental and simulation results verifies the reliability of the AW-MOPSO algorithm-optimized design and the practical application value of the filter.

5. Conclusion

This study proposes a multilayer two-dimensional material optical chiral filter design scheme based on the AW-MOPSO algorithm. By constructing a chiral performance-oriented dynamic weight adjustment mechanism, improving the velocity iteration formula, and the elite retention mechanism, precise optimization of key structural parameters such as the number of stacked layers and the twist angle is achieved, effectively balancing multiple performance requirements. Simulation and experimental results show that the designed filter achieves a stable response in the 520-680 nm visible light band. Simulation measurements show a chiral separation of 28.6 dB, an extinction ratio of 32 dB, and an insertion loss of 0.8 dB. The error between the experimental results and the simulation is less than 3%. Compared with the traditional PSO algorithm, the AW-MOPSO algorithm improves optimization efficiency by 40%, and increases separation and bandwidth by 12.3% and 18.5%, respectively, verifying the algorithm's superiority and the reliability of the design. Current research has certain limitations: the long-term stability of two-dimensional materials needs improvement, and the device fabrication cost is high, making it difficult to meet the needs of large-scale industrial applications. Future research directions can focus on exploring novel two-dimensional material systems, developing low-cost, high-stability fabrication processes, and expanding the filter's response band to the infrared region to further improve its adaptability in quantum communication, biological detection, and other fields, thus promoting the industrialization of the device.

References

[1] Gao Ximei. Matlab simulation of optical filtering experiments. Journal of Applied Technology, vol. 25, pp. 62-65, January 2025.

[2] Ye Wenni, Hu Juntao, Ying Zhihao, Wang Yishu, & Qian Yixian. Generation and control of tunable chiral structured light fields. Acta Optica Sinica, vol. 44, pp. 0826002-0826002, August 2024.

[3] Zhu Zhikang, Huang Kai, Zhang Hongzhou, & Lu Jiangang. Multi-wavelength and bandwidth tunable liquid crystal filters. Liquid Crystals and Displays, vol. 36, pp. 516-521, April 2021.

[4] Liu Yang, Liu Ning, Fang Zhenlong, Yang Li, & Wang Shanshan. All-dielectric diatomic metasurfaces with switchable chiral optical responses. Journal of Optoelectronics·Laser, vol. 36, pp. 489-498, May 2025.

[5] Zhang Yixin, Deng Shijie, & Liu Houquan. Temperature-controlled alum dioxide dual-band terahertz chiral metasurface absorber. Acta Optica Sinica, vol. 45, pp. 0926002-0926002, September 2025.

[6] Lan Xiang, Deng Qinrong, Zhang Wenting, Tang Ziyi, Hu Jie, Huang Yijia, & Li Ling. High-efficiency chiral absorber based on torsional catenary structure. Opto-Electronic Engineering, vol. 49, pp. 220157-1, October 2022.

[7] Ding Zixuan, Chen Ye, & Xu Fei. Principle and application of micro-fiber optical resonators. Opto-Electronic Engineering, vol. 49, pp. 220006-1, August 2022.

[8] Li Dan, Hu Ruiqi, Li Gongke, & Xia Ling. Research progress in Raman spectroscopy detection of chiral compounds. Journal of Analytical Testing, vol. 41, pp. 1431-1438, September 2022.

[9] Tu Youlan, Zhang Lei, Lei Menglong, Wu Shengli, Liu Haohao, Zhang Zhiyong, ... & Wang Xiangru. Synthesis and high-frequency dielectric properties of achiral β-methylbutyl polyphenyl isothiocyanate liquid crystals. Chinese Journal of Liquid Crystals and Displays, vol. 39, pp. 1735-1743, December 2024.

[10] Chen Qin, Nan Xianghong, Liang Wenyue, Zheng Qilin, Sun Zhiwei, & Wen Long. Research progress on on-chip integrated optical sensing and detection technology (invited). Infrared and Laser Engineering, vol. 51, pp. 20210671-20210671, January 2022.

[11] Bi Qianhui, Peng Yujuan, Chen Run, & Wang Shuming. Theory and application of photonic continuous domain bound states. Acta Optica Sinica, vol. 43, pp. 1623008-1623008, December 2023.

[12] Li Wenhao, Tan Yufei, Zhou Dengke, Qin Yunbai, & Yang Jiaxing. A material handling robot integrating multiple optical sensors and variable integral PID algorithm. Optics and Precision Engineering, vol. 31, pp. 3504-3516, December 2023.